https://doi.org/10.1016/j.isprsjprs.2016.02.006

Area-to-Point Regression Kriging for Pan-Sharpening

Qunming Wang [a,b,*], Wenzhong Shi [b] and Peter M. Atkinson [c,d,e]

[a] Lancaster Environment Centre, Lancaster University, Lancaster LA1 4YQ, UK

[b] Department of Land Surveying and Geo-Informatics, The Hong Kong Polytechnic University, Kowloon, Hong Kong

[c] Faculty of Science and Technology, Lancaster University, Lancaster LA1 4YR, UK

[d] School of Geography, Archaeology and Palaeoecology, Queen's University Belfast, BT7 1NN, Northern Ireland, UK

[e] Geography and Environment, University of Southampton, Highfield, Southampton SO17 1BJ, UK

*Corresponding author. E-mail: wqm11111@126.com.

Abstract: Pan-sharpening is a technique to combine the fine spatial resolution panchromatic (PAN) band with the coarse spatial resolution multispectral bands of the same satellite to create a fine spatial resolution multispectral image. In this paper, area-to-point regression kriging (ATPRK) is proposed for pan-sharpening. ATPRK considers the PAN band as the covariate. Moreover, ATPRK is extended with a local approach, called adaptive ATPRK (AATPRK), which fits a regression model using a local, non-stationary scheme such that the regression coefficients change across the image. The two geostatistical approaches, ATPRK and AATPRK, were compared to the 13 state-of-the-art pan-sharpening approaches summarized in Vivone et al. (2015) in experiments on three separate datasets. ATPRK and AATPRK produced more accurate pan-sharpened images than the 13 benchmark algorithms in all three experiments. Unlike the benchmark algorithms, the two geostatistical solutions precisely preserved the spectral properties of the original coarse data. Furthermore, ATPRK can be enhanced by a local scheme in AATRPK, in cases where the residuals from a global regression model are such that their spatial character varies locally.

Keywords: Downscaling, pan-sharpening, geostatistics, area-to-point regression kriging (ATPRK).

1. INTRODUCTION

Satellite sensors such as WorldView, QuickBird, IKONOS, SPOT and Landsat ETM+ can acquire information about the same area on the Earth's surface at different spatial resolutions and in different wavebands. For example, the WorldView multispectral sensor can acquire images in eight bands with a spatial resolution of 2 m, while the WorldView panchromatic (PAN) sensor can acquire a single band image with a spatial resolution of 0.5 m. It is of great interest to fuse such fine spatial resolution PAN band images with coarse spatial resolution multispectral bands covering the same area to generate a fine spatial resolution multispectral image. Pan-sharpening is an image fusion technique developed for this purpose. By taking full advantage of images in different wavebands from the same satellite, pan-sharpened data are able to provide more detailed land-cover/land-use (LCLU) information than the original multispectral data.

Pan-sharpening has been a lively topic in the remote sensing community and has motivated considerable research over the past decades. Several reviews on pan-sharpening approaches exist (Vivone et al., 2015; Pohl et al., 1998; Wang et al., 2005; Zhang and Mishra, 2014; Zhang, 2010). Vivone et al. (2015) reviewed some widely used pan-sharpening algorithms and categorized them into two main types, including component substitution (CS) and multiresolution analysis (MRA). The core idea of CS is to transform the original multispectral data into another space and substitute one of the components with the PAN band. Algorithms falling into this type include intensity-hue-saturation (IHS) (Tu et al., 2001; Zhou et al., 2014), Brovey transformation (Gillespie et al., 1987), principal component analysis (PCA) (Shettigara et al., 1992), Gram-Schmidt (GS) transformation (Laben and Brower, 2000), adaptive GS (GSA) (Aiazzi et al., 2007), and partial replacement adaptive component substitution (PRACS) (Choi et al., 2011). The MRA approach injects the spatial detail produced by multiresolution decomposition of the PAN band. Common MRA examples are high-pass filtering (HPF) (Chavez Jr. et al., 1991), smoothing filter-based intensity modulation (SFIM) (Liu, 2000), decimated wavelet transform using an additive injection model (Indusion) (Khan et al., 2008), *a trous* wavelet transform (ATWT) (Vivone et al., 2014), additive wavelet luminance proportional (AWLP) (Nunez et al., 1999), ATWT using the Model 2 (ATWT-M2) (Ranchin and Wald, 2000) and Model 3 (ATWT-M3) (Ranchin and Wald, 2000), generalized Laplacian pyramid (GLP) with modulation transfer function (MTF)-matched filter (MTF-GLP) (Aiazzi et al., 2006), and GLP with MTF-matched filter and multiplicative injection model (MTF-GLP-HPM) (Lee and Lee, 2010). In addition, sparse representation-based pan-sharpening approaches have also received increasing attentions (Cheng et al., 2015).

Geostatistical solutions provide another family of approaches for pan-sharpening. They have the significant advantage of preserving the spectral properties of the observed coarse images: that is, when upscaling the pan-sharpened image to the original coarse spatial resolution, the result is identical to the original one, a property referred to as perfect coherence. Pardo-Iguzquiza et al. (2006) sharpened Landsat ETM+ images with downscaling cokriging (DSCK), which treats each observed coarse band as the primary variable and the PAN band as the secondary variable. DSCK was extended with a spatially adaptive filtering scheme (Pardo-Iguzquiza et al., 2006), in which the cokriging weights change across the whole image. Tang et al. (2015) considered multiple-point statistics as a post-processing step of DSCK to increase the accuracy of pan-sharpening. Atkinson et al. (2008) extended the DSCK approach to increase the spatial resolution of the multispectral bands beyond that of any input images including the PAN band. However, the one-stage DSCK approach requires complex auto-semivariogram and cross-semivariogram modeling for each coarse band, which makes it difficult to automate (Sales et al., 2013).

Similarly to the issue defined for pan-sharpening, some other geostatistical solutions were developed for fusing MODIS bands 1-2 and bands 3-7. Specifically, Sales et al. (2013) proposed a kriging with external drift (KED) approach. KED requires only auto-semivariogram modeling for the observed coarse band and is easier to implement than DSCK (Sales et al., 2013). KED, however, suffers from expensive computational cost, as it computes kriging weights locally for each fine pixel (Sales et al., 2013). The computing time is related directly with the number of fine pixels to be predicted. In view of this, in previous work (Wang et al., 2015), we proposed an area-to-point regression kriging (ATPRK) approach for MODIS image downscaling. ATPRK is faster than KED and more user-friendly than DSCK. Moreover, ATPRK can incorporate readily other supplementary data for possible enhancement.

The objective of fusing MODIS bands 1-2 and bands 3-7 is physically different from that for pan-sharpening other data (e.g., very high resolution (VHR) images). First, MODIS bands 1-2 and bands 3-7 are not acquired in the same spectral range, while the PAN and corresponding multispectral bands of the satellite sensor are almost in the same spectral range. Thus, the PAN band can, theoretically, provide more relevant fine spatial resolution information for sharpening. Second, due to the differences in spatial resolution, the spatial content in MODIS data is generally different from that in Landsat and VHR images. The 500 m MODIS images are commonly used for global monitoring of large scale LCLU information, such as in relation to vegetation, water and snow cover. The 2-4 m VHR images are used generally for local detection or monitoring of small-sized LCLU objects of interest, including impervious surfaces, urban objects, and military targets (such as planes and ships).

In this paper, based on encouraging performance in relation to MODIS image fusion (Wang et al., 2015) and its theoretical advantages, ATPRK is proposed for pan-sharpening. ATPRK models the overall trend in the target variables (i.e., fine spatial resolution pixels to be predicted) by regression of the primary variables (i.e., coarse spatial resolution bands to be downscaled) on a covariate (i.e., the PAN band degraded to coarse spatial resolution) (Hengl et al., 2004,2007). Area-to-point kriging (ATPK) (Kyriakidis and Yoo, 2005; Kyriakidis, 2004; Atkinson, 2013) is then performed as the second step to downscale the coarse residuals from the regression process, the output of which are finally added back to the regression predictions to produce pan-sharpened images.

In Wang et al. (2015), the regression model was built using the global image (i.e., all pixels in the coarse band and the PAN band) and the regression coefficients were fixed for each coarse pixel. However, the spatial structure of LCLU sometimes demands a non-stationary model, that is, with parameters that vary spatially (Wang et al., 2014). For example, in the studied image, some large regions may be dominated by impervious surfaces in urban areas, while some other large regions may be mainly covered by vegetation. The obvious difference in spectra of the LCLU classes will lead to the requirement for non-stationary parameters and, thus, the relationship between the coarse band and the PAN band may not be sufficiently characterized by a single, global regression model. To this end, a secondary objective of this paper was to extend the recently developed ATPRK with a spatially adaptive scheme, called adaptive ATPRK (AATPRK). AATPRK characterizes the relationship between each coarse band and the PAN band using the local spatial structure and a regression model fitted on a per-coarse pixel basis.

The contributions of this paper are, thus, threefold.

1) A new geostatistical approach, ATPRK, is applied for pan-sharpening VHR images for the first time. The problem of pan-sharpening VHR images is an important one, is commonly encountered in remote sensing, and is different from the fusion of medium spatial resolution images (e.g., MODIS images), as mentioned above.
2) A systematic comparison between ATPRK and the state-of-the-art approaches to pan-sharpening, as introduced above.
3) Extension of ATPRK with the proposed non-stationary spatially adaptive scheme, that is, AATPRK.

The remainder of this paper is organized into four sections. Section 2 introduces the principles of ATPRK and AATPRK in detail. In Section 3, the experimental results for two WorldView-2 datasets and one Landsat ETM+ dataset are provided to demonstrate the applicability of ATPRK and AATPRK in pan-sharpening. Section 4 further discusses the proposed approach, followed by a conclusion in Section 5.

2. METHODS

Let $Z_C^l(\mathbf{x}_i)$ be the measurements (i.e., gray value) of pixel *C* centered at $\mathbf{x}_i$ (i=1,…,M, where M is the number of pixels) in coarse band l (l=1,…,B, where B is the number of bands), and $Z_F(\mathbf{x}_j)$ be the measurements of pixel *F* centered at $\mathbf{x}_j$ (j=1,…, MG^2, where G is the spatial resolution (zoom) ratio between the coarse and PAN bands) in the PAN band. The notations *F* and *C* denote the fine and coarse pixels, respectively. The objective of pan-sharpening is to predict target variables $Z_F^l(\mathbf{x})$ for all fine pixels in all *B* coarse bands.

2.1.ATPRK

ATPRK contains two steps: regression modelling and ATPK-based residual downscaling. Suppose $\hat{Z}_{F1}^l(\mathbf{x})$ and $\hat{Z}_{F2}^l(\mathbf{x})$ are predictions of the regression and ATPK parts, the ATPRK prediction is

$$\hat{Z}_F^l(\mathbf{x}) = \hat{Z}_{F1}^l(\mathbf{x}) + \hat{Z}_{F2}^l(\mathbf{x})\,. \tag{1}$$

Details of the calculation processes are given in the following.

1) Regression modelling. In ATPRK, the covariate (i.e., the PAN band) is used to predict the overall trend of $Z_F^l(\mathbf{x})$ and is critical in pan-sharpening, as it provides valuable finer spatial resolution textural information than the observed coarse data. The regression step aims to make full use of the fine spatial resolution textural information in the PAN band by characterizing the relationship between each coarse band and the PAN band.

The PAN band Z_F is first upscaled to Z_C to match the spatial resolution of the coarse bands

$$Z_C = h_C(\mathbf{x}) * Z_F(\mathbf{x}) = \int h_C(\mathbf{x}-\mathbf{y}) Z_F(\mathbf{y}) \mathrm{d}\mathbf{y} \tag{2}$$

where $h_C(\mathbf{x})$ is the point spread function (PSF) for the PAN band and * is the convolution operator.

The relationship between Z_C and each coarse band l is then modelled by linear regression

$$Z_C^l(\mathbf{x}) = a_l Z_C(\mathbf{x}) + b_l + R(\mathbf{x}) . \tag{3}$$

In (3), $R(\mathbf{x})$ is a residual term. The two coefficients a_l and b_l can be estimated by ordinary least squares (Kitanidis, 1994). Based on the assumption of scale-invariance, a_l and b_l estimated at coarse spatial resolution in (3) is used for regression prediction at fine spatial resolution. Specifically, with the available fine spatial resolution PAN band, the regression prediction at a specific location $\mathbf{x}_0$ at fine spatial resolution, that is, $\hat{Z}_{F1}^l(\mathbf{x}_0)$, is calculated as

$$\hat{Z}_{F1}^l(\mathbf{x}_0) = a_l Z_F(\mathbf{x}_0) + b_l . \tag{4}$$

2) ATPK-based residual downscaling. The regression model in (3) does not hold strictly for all coarse pixels and there are generally residuals from the model. The coarse residual in band l, denoted as $Z_{C2}^l(\mathbf{x})$, is

$$Z_{C2}^l(\mathbf{x}) = R(\mathbf{x}) = Z_C^l(\mathbf{x}) - [a_l Z_C(\mathbf{x}) + b_l] . \tag{5}$$

The regression process alone is insufficient for sharpening, as it does not make full use of the spectral information in the observed coarse data. ATPK-based residual downscaling is performed as a complement to the regression step to honor the spectral properties of the coarse data. ATPK is a downscaling technique that predicts values on a support smaller than that of the original data (Kyriakidis and Yoo, 2005; Kyriakidis, 2004; Atkinson, 2013). It is different from conventional (centroid-based) kriging, which treats each observation as a centroid and ignores the spatial support of the observation. ATPK accounts for the size of support, spatial correlation, and the PSF of the sensor. In addition, an important advantage of ATPK is its coherence property (Kyriakidis and Yoo, 2005; Kyriakidis, 2004), that is, it can perfectly preserve the spectral properties of the observed coarse data.

Based on ATPK, the fine residual at a specific location $\mathbf{x}_0$, $\hat{Z}_{F2}^{l}(\mathbf{x}_0)$, is a linear combination of the observed coarse residuals

$$\hat{Z}_{F2}^{l}(\mathbf{x}_0)=\sum_{i=1}^{N}\lambda_i Z_{C2}^{l}(\mathbf{x}_i),\ \text{s.t.}\ \sum_{i=1}^{N}\lambda_i=1 \tag{6}$$

where λ_i is the weight for the ith coarse residual centered at $\mathbf{x}_i$ and N is the number of coarse observations used in the prediction, such as the N=5×5 window of coarse pixels surrounding the fine pixel. Fig. 1 summarizes the whole calculation process in ATPK-based residual downscaling.

The N weights $\{\lambda_1,...,\lambda_N\}$ in (6) are calculated by minimizing the prediction error variance and the corresponding kriging matrix is

$$\begin{bmatrix} \gamma_{CC}^{l}(\mathbf{x}_1,\mathbf{x}_1) & \cdots & \gamma_{CC}^{l}(\mathbf{x}_1,\mathbf{x}_N) & 1 \\ \vdots & \ddots & \vdots & \vdots \\ \gamma_{CC}^{l}(\mathbf{x}_N,\mathbf{x}_1) & \cdots & \gamma_{CC}^{l}(\mathbf{x}_N,\mathbf{x}_N) & 1 \\ 1 & \cdots & 1 & 0 \end{bmatrix}\begin{bmatrix} \lambda_1 \\ \vdots \\ \lambda_N \\ \theta \end{bmatrix}=\begin{bmatrix} \gamma_{FC}^{l}(\mathbf{x}_0,\mathbf{x}_1) \\ \vdots \\ \gamma_{FC}^{l}(\mathbf{x}_0,\mathbf{x}_N) \\ 1 \end{bmatrix}. \tag{7}$$

In (7), the term $\gamma_{CC}^{l}(\mathbf{x}_i,\mathbf{x}_j)$ is the coarse-to-coarse residual semivariogram between coarse pixels centered at $\mathbf{x}_i$ and $\mathbf{x}_j$ in band l, $\gamma_{FC}^{l}(\mathbf{x}_0,\mathbf{x}_j)$ is the fine-to-coarse residual semivariogram between fine and coarse pixels centered at $\mathbf{x}_0$ and $\mathbf{x}_j$ in band l, and θ is the Lagrange multiplier.

Let $\mathbf{s}$ be the Euclidean distance between the centroids of any two pixels, $\gamma_{FF}^{l}(\mathbf{s})$ be the fine-to-fine residual semivariogram between two fine pixels, and $h_C^{l}(\mathbf{s})$ be the PSF for band l. $\gamma_{CC}^{l}(\mathbf{s})$ and $\gamma_{FC}^{l}(\mathbf{s})$ in (7) are calculated by convoluting $\gamma_{FF}^{l}(\mathbf{s})$ with the PSF $h_C^{l}(\mathbf{s})$ as follows

$$\gamma_{FC}^{l}(\mathbf{s})=\gamma_{FF}^{l}(\mathbf{s})*h_C^{l}(\mathbf{s}) \tag{8}$$

$$\gamma_{CC}^{l}(\mathbf{s})=\gamma_{FF}^{l}(\mathbf{s})*h_C^{l}(\mathbf{s})*h_C^{l}(-\mathbf{s}). \tag{9}$$

By assuming that the coarse pixel value is the average of the fine pixel values within it, the PSF is

$$h_C(\mathbf{x}) = \begin{cases} \dfrac{1}{S_C}, & \text{if } \mathbf{x} \in C(\mathbf{x}) \\ 0, & \text{otherwise} \end{cases} \tag{10}$$

where S_C is the size of pixel C and $C(\mathbf{x})$ is the spatial support of pixel C centered at $\mathbf{x}$. Given the PSF in (10), the calculation of $\gamma_{FC}^{l}(\mathbf{x}_0, \mathbf{x}_j)$ and $\gamma_{CC}^{l}(\mathbf{x}_i, \mathbf{x}_j)$ are simplified as

$$\gamma_{FC}^{l}(\mathbf{x}_0, \mathbf{x}_j) = \frac{1}{\sigma}\sum_{m=1}^{\sigma} \gamma_{FF}^{l}(\mathbf{s}_m) \tag{11}$$

$$\gamma_{CC}^{l}(\mathbf{x}_i, \mathbf{x}_j) = \frac{1}{\sigma^2}\sum_{m=1}^{\sigma}\sum_{m'=1}^{\sigma} \gamma_{FF}^{l}(\mathbf{s}_{mm'}) \tag{12}$$

in which $\sigma = G^2$ is the pixel size ratio between the coarse and fine pixels, $\mathbf{s}_m$ is the distance between the centroid $\mathbf{x}_0$ of fine pixel F and the centroid of any fine pixel within the coarse pixel C centered at $\mathbf{x}_j$, and $\mathbf{s}_{mm'}$ is the distance between the centroid of any fine pixel within the coarse pixel centered at $\mathbf{x}_i$ and the centroid of any fine pixel within the coarse pixel centered at $\mathbf{x}_j$. The fine-to-fine residual semivariogram $\gamma_{FF}^{l}(\mathbf{s})$ is derived by deconvolution of the coarse residual semivariogram of the coarse residual of band l (denoted as $\gamma_{C}^{l}(\mathbf{s})$, see (13)).

$$\gamma_{C}^{l}(\mathbf{s}) = \frac{1}{2N(\mathbf{s})}\sum_{n=1}^{N(\mathbf{s})} [Z_{C2}^{l}(\mathbf{x}) - Z_{C2}^{l}(\mathbf{x}+\mathbf{s})]^2 \tag{13}$$

where $N(\mathbf{s})$ is the number of paired pixels at a specific lag $\mathbf{s}$ from the center pixel $\mathbf{x}$.

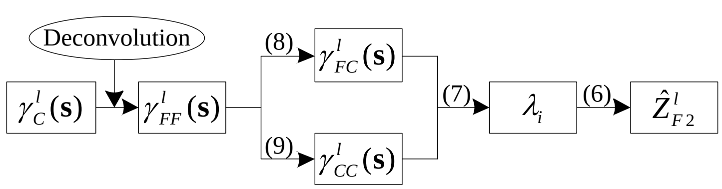

Fig. 1. Calculation process of ATPK-based residual downscaling.

As for the deconvolution process, the empirical approach in Wang et al. (2015) was applied in this paper. We suppose the semivariogram function of $\gamma_{FF}^{l}(\mathbf{s})$ can be characterized by two parameters, sill and range, and there is zero nugget effect. First, a candidate pool of $\gamma_{FF}^{l}(\mathbf{s})$ is generated by referring to the known $\gamma_{C}^{l}(\mathbf{s})$. For each parameter of $\gamma_{FF}^{l}(\mathbf{s})$, two multipliers are defined empirically to generate an interval for selecting the optimal one. More precisely, in this paper, the interval for punctual sill selection was set to between 1 and 3 times that of the sill of $\gamma_{C}^{l}(\mathbf{s})$, while the interval for punctual range selection was set to between 0.5 and 2.5 times that of the range of $\gamma_{C}^{l}(\mathbf{s})$. The selection step was 0.1. Second, each $\gamma_{FF}^{l}(\mathbf{s})$ characterized by the two parameters is convolved to the regularized semivariogram, $\gamma_{C}^{R}(\mathbf{s})$, by $\gamma_{C}^{R}(\mathbf{s})=\gamma_{CC}^{l}(\mathbf{s})-\gamma_{CC}^{l}(0)$. Finally, the optimal $\gamma_{FF}^{l}(\mathbf{s})$ is determined as the one with the parameter combination leading to the smallest difference between $\gamma_{C}^{R}(\mathbf{s})$ and $\gamma_{C}^{l}(\mathbf{s})$.

2.2.AATPRK

ATPRK uses the fixed regression model (characterized by two coefficients a_l and b_l in (3)) fitted using the entire coarse image and PAN image. The single, global regression model may not be able to satisfactorily deal with local variation, where the relation between the coarse and PAN bands changes from site to site. In this case, the coarse residuals may be larger than is necessary, placing a lot of emphasis on the geostatistics-based approach (i.e., ATPK) for downscaling. Moreover, if the residuals from the global regression model are such that their spatial character varies locally then presents challenges for downscaling using a spatially stationary ATPK model. This encourages the development of an adaptive, non-stationary ATPRK approach (i.e., AATPRK) in this paper to enhance the performance of pan-sharpening.

In AATPRK, for each coarse pixel, a linear regression model is fitted using the coarse and (upscaled) PAN pixels within a $W \times W$ local window. The regression coefficients are estimated on a coarse pixel basis and they are functions of the pixel locations. The relationship in (3) is, thus, modified to

$$Z_C^l(\mathbf{x}) = a_l(\mathbf{x})Z_C(\mathbf{x}) + b_l(\mathbf{x}) + R(\mathbf{x}). \tag{14}$$

Correspondingly, for any fine pixel in band l, say, a fine pixel centered at $\mathbf{x}_0$, the regression prediction $\hat{Z}_{F1}^l(\mathbf{x}_0)$ becomes

$$\hat{Z}_{F1}^l(\mathbf{x}_0) = a_l(\mathbf{X}_0)Z_F(\mathbf{x}_0) + b_l(\mathbf{X}_0) \tag{15}$$

where $\mathbf{X}_0$ is the center of the coarse pixel in which the fine pixel centered at $\mathbf{x}_0$ falls.

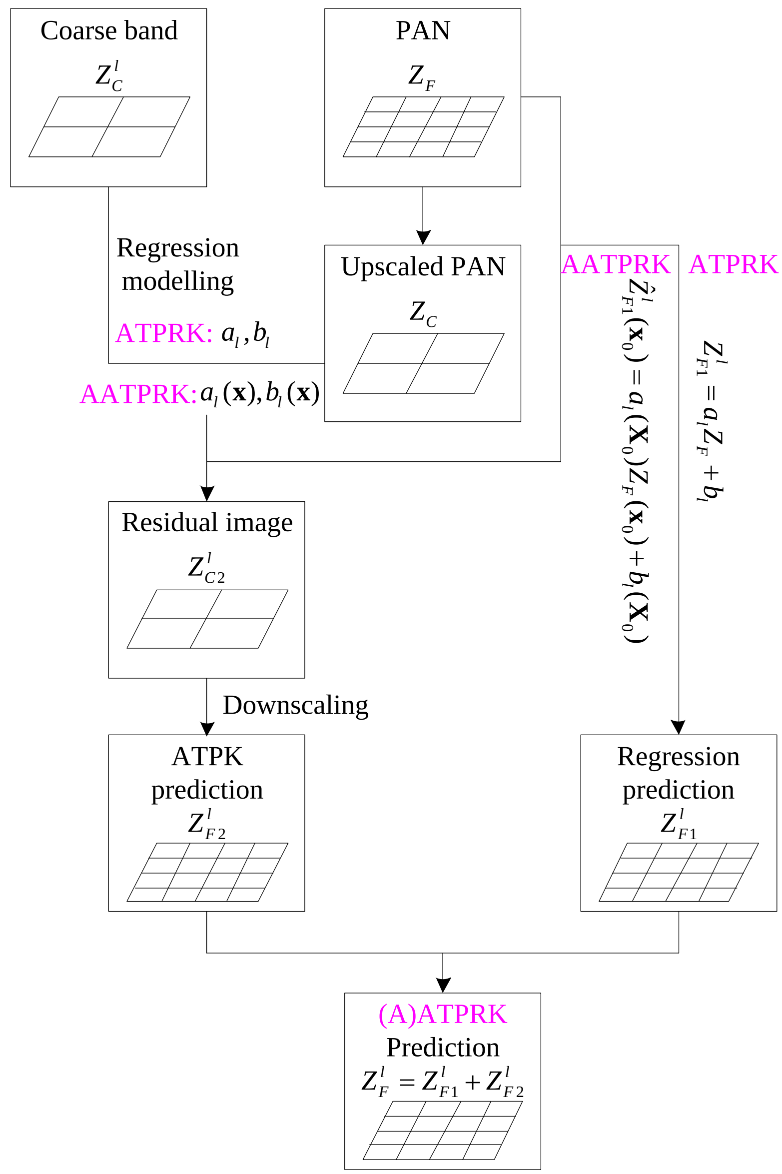

Fig. 2. Flowchart of ATPRK and AATPRK.

After the regression modelling step, coarse residual images are obtained for each coarse band. Similarly, ATPK is performed to downscale the residual images to the target fine spatial resolution residuals $\hat{Z}^l_{F2}(\mathbf{x})$ according to (6). The ATPK prediction is finally added back to the regression prediction in (15) to achieve the AATPRK prediction. Fig. 2 sketches the flowchart of ATPRK and AATPRK.

3. EXPERIMENTS

3.1.Datasets

Three datasets, including two WorldView-2 datasets and one Landsat ETM+ dataset, were used to examine the performances of ATPRK and AATPRK in pan-sharpening.

The WorldView-2 datasets contain eight multispectral bands with a spatial resolution of 2 m and a PAN band with a spatial resolution of 0.5 m. Both WorldView-2 multispectral images contain 500 by 500 pixels, whereas the PAN bands contain 2000 by 2000 pixels. Both datasets were acquired in April, 2011. One covers a suburb area of Hong Kong, while the other covers an urban area of Shenzhen, China. Fig. 3(a) and Fig. 3(b) show the false color composite of the two WorldView-2 multispectral images.

(a)

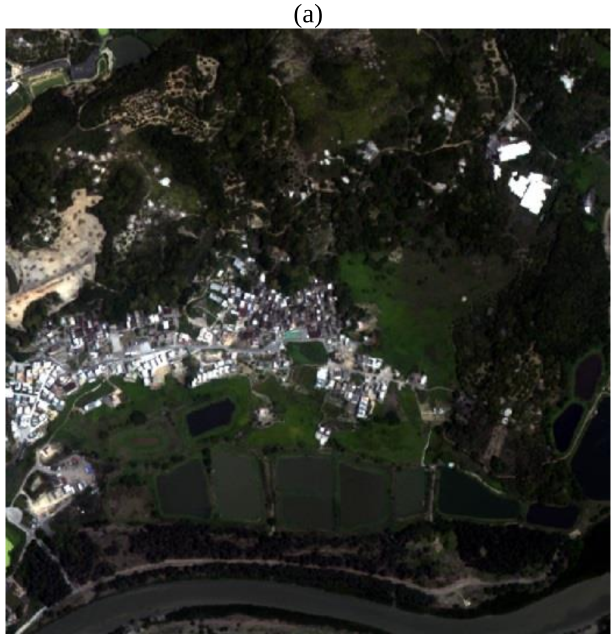

(b)

(c)

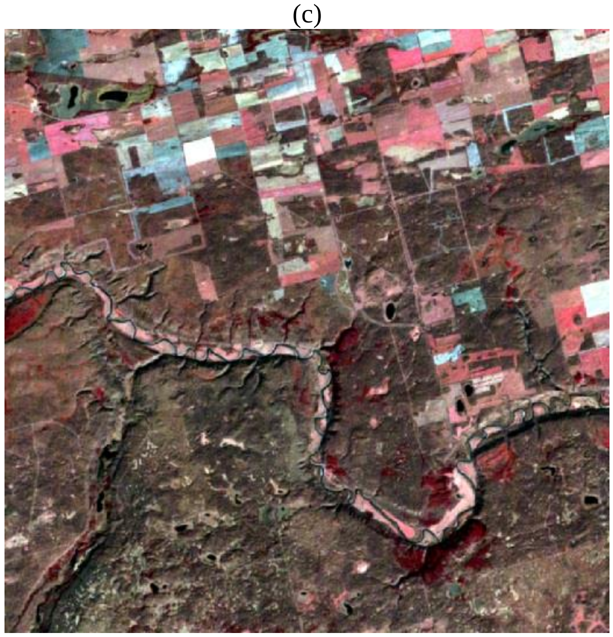

Fig. 3. Datasets used in the experiments (bands 4, 3 and 2 as RGB). (a) The 2 m WorldView-2 dataset of Hong Kong (500 by 500 pixels). (b) The 2 m WorldView-2 dataset of Shenzhen (500 by 500 pixels). (b) The 30 m Landsat ETM+ dataset of Alberta (512 by 512 pixels).

The Landsat dataset covers a 15 km by 15 km area in Alberta in Canada. The 30 m green, red, and near-infrared bands (i.e., bands 2, 3, and 4) and 15 m PAN band 8 were used in the experiments. The 30 m bands and PAN band contain 512 by 512 and 1024 by 1024 pixels, respectively. The false color composite of the Landsat image is shown in Fig. 3(c).

3.2.Experimental setup

The 2 m WorldView-2 multispectral bands can be fused with the 0.5 m PAN band to produce 0.5 m pan-sharpened WorldView-2 images, while the 30 m Landsat ETM+ multispectral bands can be fused with the 15 m PAN bands to produce 15 m pan-sharpened images. Following this strategy, however, no reference at 0.5 m and 15 m can be used to examine the sharpened results objectively. To ensure the existence of perfect fine spatial resolution reference images, the 2 m WorldView-2 multispectral bands and 30 m Landsat ETM+ multispectral bands were upscaled by a factor to synthesize coarse images, see the upscaling model in (2). More precisely, the 2 m WorldView-2 multispectral bands and 0.5 m PAN band were simultaneously upscaled by a factor of four to create 8 m multispectral bands and 2 m PAN bands. The pan-sharpening approaches were then implemented to fuse the 8 m multispectral bands and the 2 m PAN band to produce 2 m multispectral bands, which could be compared to the original 2 m multispectral bands for objective assessment. Similarly, for the Landsat ETM+ dataset, all bands were upscaled by a factor of two to synthesize 60 m multispectral bands and a 30 m PAN band. The task of ATPRK- and AATPRK-based pan-sharpening was then to predict the 30 m multispectral bands, based on the assumption that the PSF in (10) is known.

The two geostatistical solutions, ATPRK and AATPRK, were compared to 13 state-of-the-art algorithms summarized in Vivone et al. (2015) to illustrate the benefits of the new pan-sharpening approaches. They are PCA, GS, GSA, PRACS, HPF, SFIM, Indusion, ATWT, AWLP, ATWT-M2, ATWT-M3, MTF-GLP, and MTF-GLP-HPM. Six indices were used for quantitative evaluation, including the root mean square error (RMSE), correlation coefficient (CC), universal image quality index (UIQI) (Wang and Bovik, 2002), relative global-dimensional synthesis error (ERGAS) (Ranchin and Wald, 2000), spectral angle mapper (SAM) and coherence. For RMSE, CC and UIQI, they were first calculated for each band, and then the values for all bands were averaged. Regarding SAM, values for spectra of all pixels were first calculated and then averaged.

As mentioned in Wald et al. (1997), any synthetic image, once degraded to its original spatial resolution, should be as close as possible to the original image. Coherence (quantified by the CC) is an index measuring the relation between the observed coarse image and the coarse image obtained by upscaling the pan-sharpened image. For each multispectral band, a coherence value was calculated and the values for all bands were averaged.

3.3.Experiments on the WorldView-2 datasets

1) Hong Kong WorldView-2 dataset. As mentioned in Section 2.2, the difference between ATPRK and AATPRK lies in regression modelling. The former uses the entire image to build a single linear regression model, whereas the latter fits the regression model in units of coarse pixels. In this section, a 5 by 5 local window (i.e., W=5) for regression modelling in AATPRK was considered. The influence of the local window size W can be found in the later Section 3.3 *3)*.

Table 1 lists the regression coefficients of ATRPK and Fig. 4 shows the regression coefficients of AATRPK for bands 1-8. As can be observed from Fig. 4, for each multispectral band, both coefficients change across the entire image, and they are functions of the pixel locations. The changes are large in some bands. For example, the change ranges of a_l are much larger in bands 7 and 8. The coarse residuals for bands 1-8 from the regression models in ATPRK and AATPRK are shown in Fig. 5. It is obvious that by using the local regression model, AATPRK greatly decreased the residuals in ATPRK. This is particularly noticeable in band 4, where the water (in ponds and river) pixels in ATPRK show residuals over 40 (in units of DN) but in AATPRK the residuals decreased to be between -5 and 5 (in units of DN). The residual image of AATPRK visually shows less local variation than that of ATPRK. This is of great significance for the geostatistical solution (i.e., ATPK) to downscaling the residuals, which is performed based on the stationarity assumption. The results in Fig. 5 and Fig. 6 demonstrate that in the Hong Kong WorldView-2 dataset, the relation between the coarse and PAN bands changes from area-to-area and it cannot be characterized sufficiently by a fixed regression model.

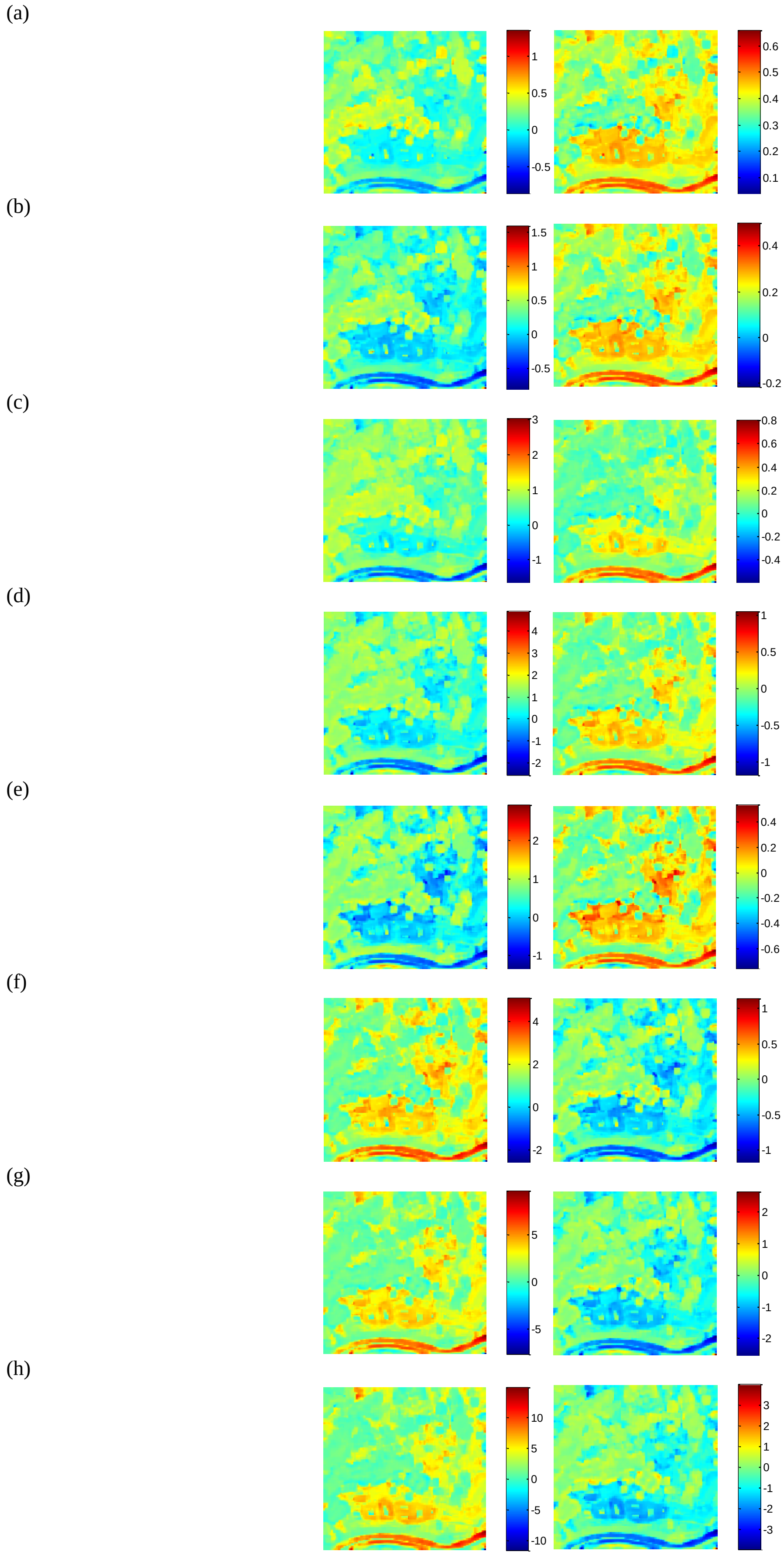

Fig. 4. Regression coefficients of AATPRK for the Hong Kong WorldView-2 multispectral bands. Left: a_l. Right: b_l. (a)-(h) Bands 1-8.

(a)
(b)
(c)
(d)
(e)
(f)
(g)
(h)

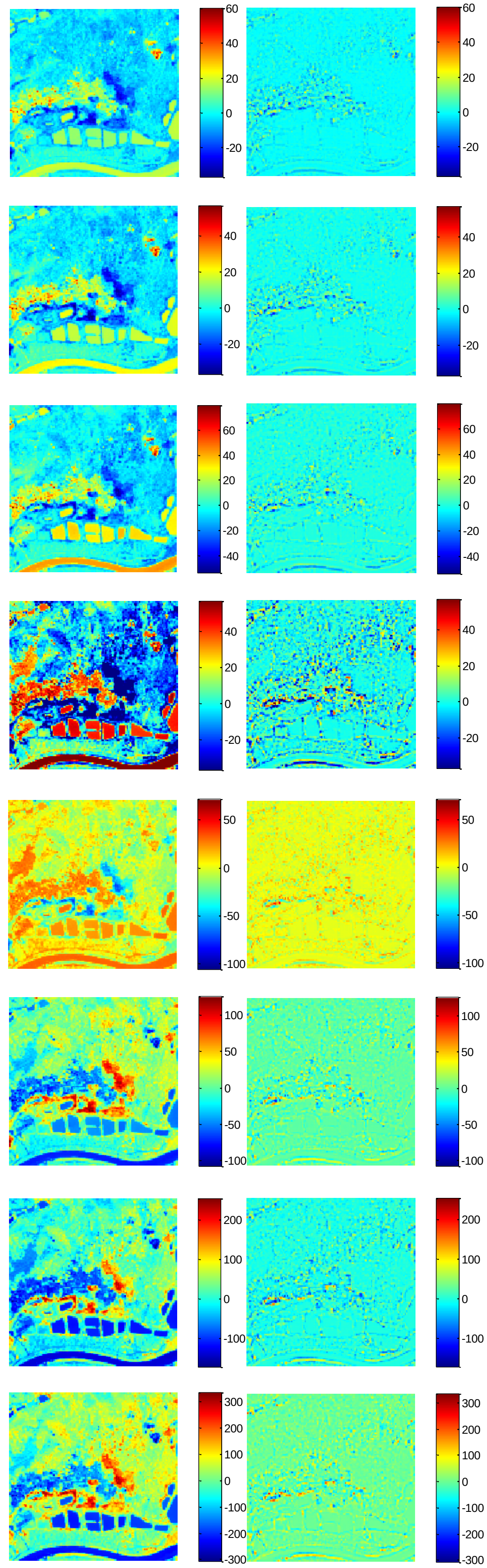

Fig. 5. Coarse residuals (the units are DN) from the regression models in ATPRK and AATPRK for the Hong Kong WorldView-2 multispectral bands. Left: ATPRK. Right: AATPRK. (a)-(h) Bands 1-8.

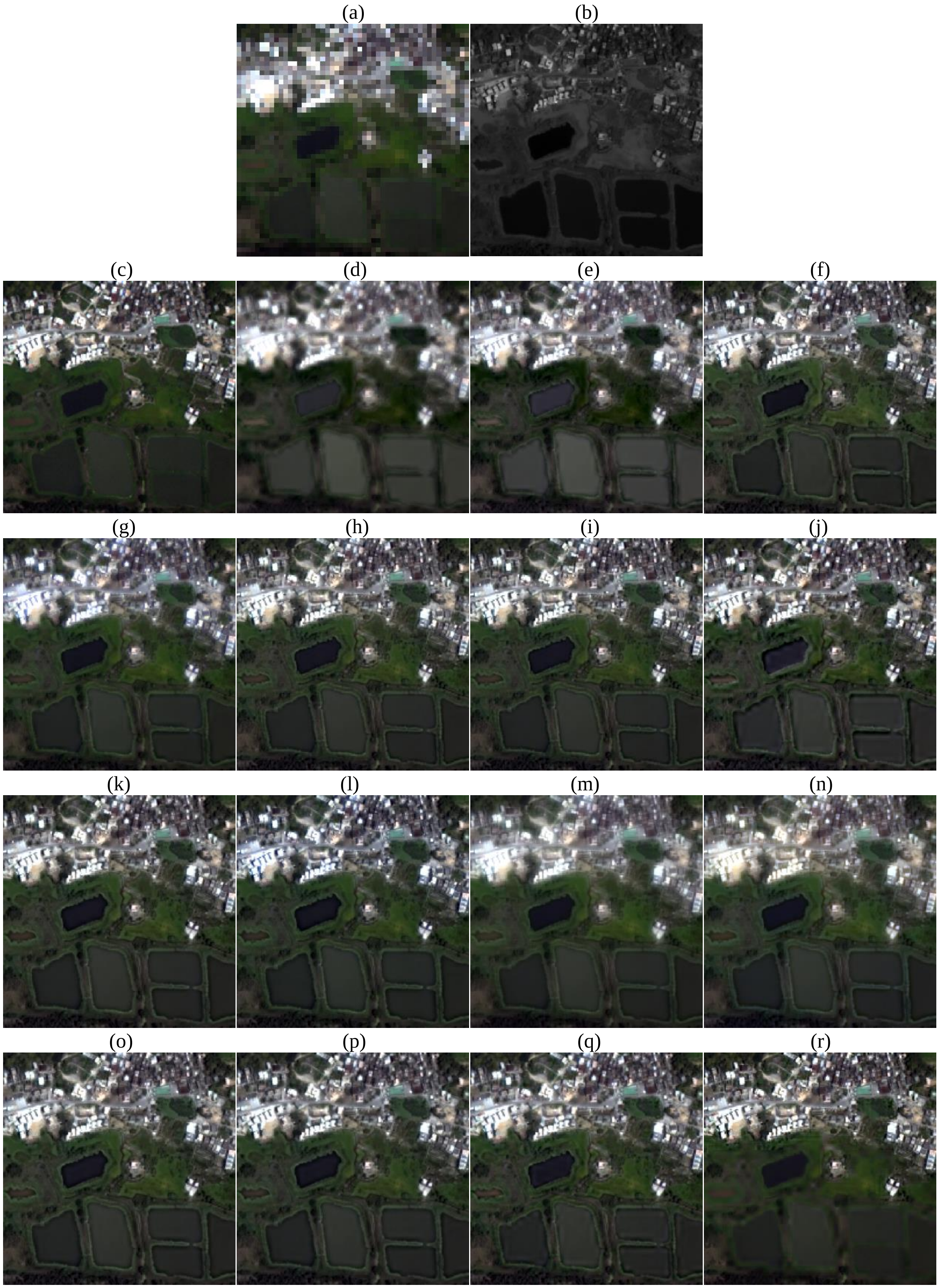

Fig. 6. Pan-sharpening results for the Hong Kong WorldView-2 dataset (bands 4, 3 and 2 as RGB). (a) 8 m coarse image. (b) 2 m PAN image. (c) 2 m reference image. (d) PCA. (e) GS. (f) GSA. (g) PRACS. (h) HPF. (i) SFIM. (j) Indusion. (k) ATWT. (l) AWLP. (m) ATWT-M2. (n) ATWT-M3. (o) MTF-GLP. (p) MTF-GLP-HPM. (q) ATPRK. (r) AATPRK.

Table 1 Regression coefficients of ATPRK for the Hong Kong WorldView-2 multispectral bands (l denotes the band number)

	l=1	l=2	l=3	l=4	l=5	l=6	l=7	l=8
a_l	0.3184	0.3746	0.8117	1.1681	0.7304	1.3041	1.0081	1.5319
b_l	0.3514	0.1511	0.0758	-0.0529	-0.0867	-0.0367	-0.0003	-0.0229

Table 2 Quantitative assessment of the pan-sharpening methods for the Hong Kong WorldView-2 dataset

	RMSE	CC	ERGAS	UIQI	SAM(°)	Coherence
Ideal	0	1	0	1	0	1
PCA	34.9921	0.8697	2.9433	0.8640	0.0859	0.8965
GS	21.5963	0.9528	1.7772	0.9425	0.0540	0.9771
GSA	15.3475	0.9744	1.2819	0.9735	0.0427	0.9968
PRACS	16.6791	0.9678	1.4437	0.9645	0.0446	0.9978
HPF	16.2255	0.9700	1.3533	0.9697	0.0436	0.9967
SFIM	15.3575	0.9724	1.2744	0.9720	0.0410	0.9971
Indusion	19.1221	0.9587	1.5978	0.9581	0.0496	0.9861
ATWT	16.5085	0.9699	1.3821	0.9699	0.0439	0.9940
AWLP	17.5778	0.9669	1.4737	0.9662	0.0464	0.9931
ATWT-M2	19.9606	0.9556	1.6435	0.9474	0.0508	0.9873
ATWT-M3	20.1494	0.9579	1.6668	0.9509	0.0533	0.9882
MTF-GLP	16.6121	0.9699	1.3941	0.9699	0.0443	0.9943
MTF-GLP-HPM	15.6441	0.9725	1.3036	0.9723	0.0411	0.9948
ATPRK	14.0129	0.9776	1.1768	0.9773	0.0414	**1**
AATPRK	**13.4886**	**0.9794**	**1.1322**	**0.9793**	**0.0387**	**1**

Fig. 6 displays the pan-sharpening results of the two geostatistical approaches (i.e., ATPRK and AATPRK) as well as the 13 benchmark approaches. For clearer visual comparison between the results, the results of a 200 by 200 sub-area are shown. All pan-sharpening results are visually clearer than the 8 m coarse image. The PCA, GS, PRACS, ATWT-M2 and ATWT-M3 approaches produced sharpened images with ambiguous "white" pixels in the areas covered by the houses. Although GSA, HPF, SFIM, Indusion, ATWT, AWLP, MTF-GLP, MTF-GLP-HPM and ATPRK can satisfactorily restore the "white" pixels, the "dark" pixels in the areas covered by water (in ponds) look different from the reference image. Compared to these approaches, AATPRK is advantageous in reproducing the house and water pixels in the entire study area.

Table 2 lists the quantitative assessment results for the 15 pan-sharpening approaches. The ideal value for each index is also provided for convenience of inter-comparison. Checking the results, the two geostatistical approaches (i.e., ATPRK and AATPRK) outperform the 13 state-of-the-art algorithms. The RMSE, CC, ERGAS, UIQI and SAM of ATPRK and AATPRK are closer to the ideal values. Moreover, the coherence values of ATPRK and AATPRK reach the ideal value 1, suggesting that they have the characteristic of perfect coherence with the original coarse data.

Furthermore, using the local regression model, AATPRK produced smaller RMSE, ERGAS and SAM values and greater CC and UIQI values than the ATPRK approach. The visual and quantitative assessment in this experiment reveals that the advanced ATPRK approach can be further enhanced with the local scheme in AATPRK.

2) Shenzhen WorldView-2 dataset. The pan-sharpening results for a 200 by 200 sub-area of the Shenzhen WorldView-2 dataset are shown in Fig. 7. The results of the PCA, GS, PRACS, AWLP, ATWT-M2 and ATWT-M3 approaches produced noticeable spectral distortion. Some other approaches, such as ATWT and Indusion, produced less obvious spectral distortion, but cannot satisfactorily delineate the boundaries of LCLU objects. ATPRK and AATPRK have satisfactory performances in preserving the spectral properties and delineating the boundaries for the homogeneous landscape (e.g., large-size buildings) and the texture of heterogeneous pixels (e.g., small-size cars in the scene).

The quantitative assessment is shown in Table 3. Again, both ATPRK and AATPRK are more accurate than the 13 benchmark algorithms in terms of all six indices. In this experiment, however, it should be noted that ATPRK was not enhanced by AATPRK but they produced comparable accuracies. This is because the studied scene is a highly developed urban area that is almost completely covered by impervious surfaces (e.g., buildings and roads). Compared to the previous studied area in Hong Kong where multiple LCLU materials (such as houses, vegetation and water) exist, this area is more conducive to being characterized satisfactorily by a stationary model. In this case, the single regression model in ATPRK may be sufficient and, thus, the local scheme would not impart extra benefits.

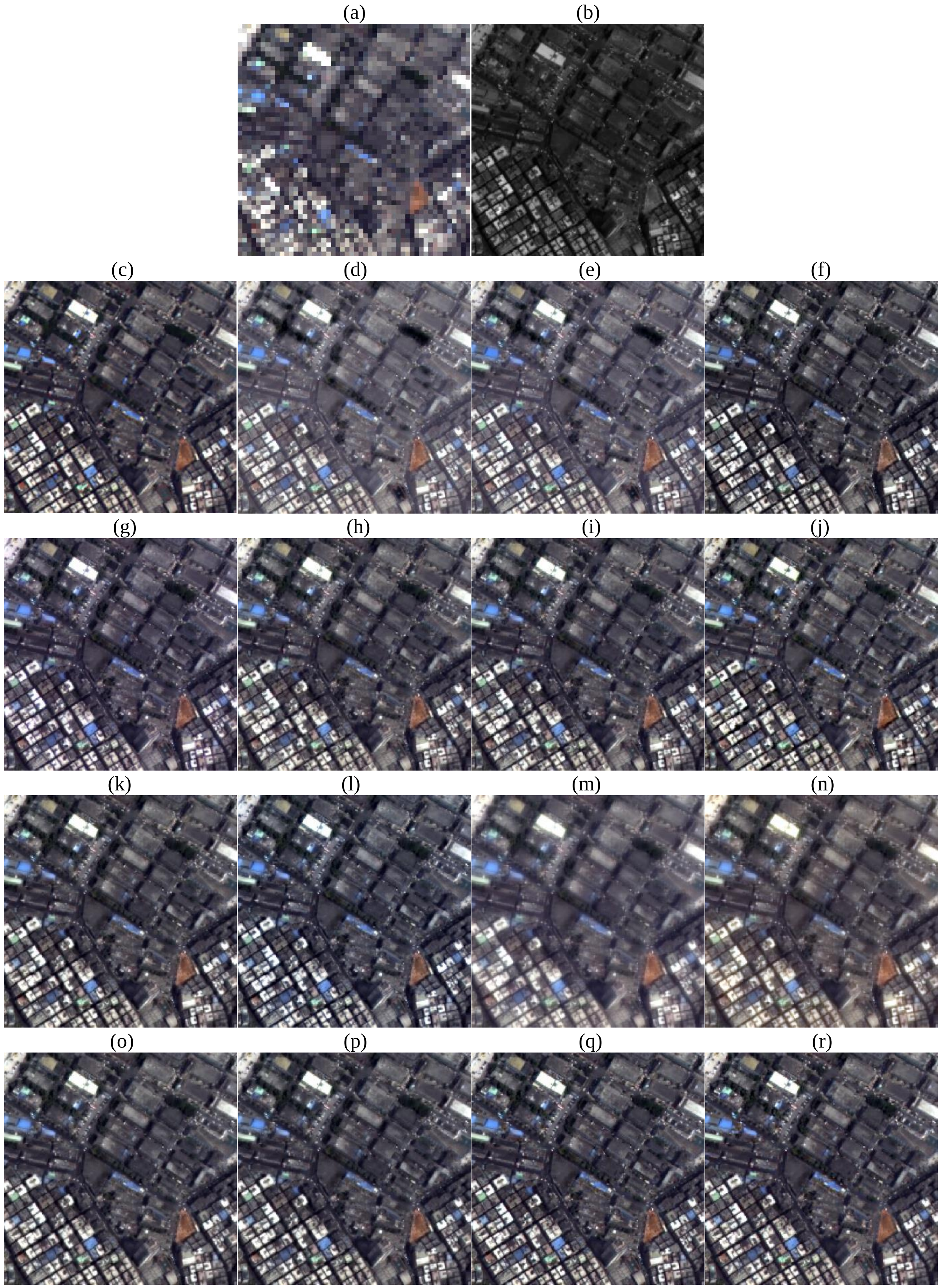

Fig. 7. Pan-sharpening results for the Shenzhen WorldView-2 dataset (bands 4, 3 and 2 as RGB). (a) 8 m coarse image. (b) 2 m PAN image. (c) 2 m reference image. (d) PCA. (e) GS. (f) GSA. (g) PRACS. (h) HPF. (i) SFIM. (j) Indusion. (k) ATWT. (l) AWLP. (m) ATWT-M2. (n) ATWT-M3. (o) MTF-GLP. (p) MTF-GLP-HPM. (q) ATPRK. (r) AATPRK.

Table 3 Quantitative assessment of the pan-sharpening methods for the Shenzhen WorldView-2 dataset

	RMSE	CC	ERGAS	UIQI	SAM(°)	Coherence
Ideal	0	1	0	1	0	1
PCA	23.3618	0.9513	1.9373	0.9235	0.0487	0.9702
GS	21.7870	0.9613	1.8135	0.9326	0.0471	0.9818
GSA	19.3931	0.9670	1.5653	0.9575	0.0453	0.9931
PRACS	18.2151	0.9616	1.6895	0.9539	0.0498	0.9969
HPF	18.0603	0.9627	1.5157	0.9596	0.0433	0.9967
SFIM	18.0210	0.9629	1.5172	0.9597	0.0433	0.9966
Indusion	19.9049	0.9527	1.6394	0.9489	0.0442	0.9772
ATWT	17.4306	0.9645	1.4642	0.9637	0.0426	0.9945
AWLP	18.3943	0.9605	1.5620	0.9575	0.0450	0.9934
ATWT-M2	25.5093	0.9371	2.0970	0.9074	0.0527	0.9789
ATWT-M3	24.2243	0.9466	2.0431	0.9221	0.0561	0.9819
MTF-GLP	16.8026	0.9669	1.4172	0.9662	0.0422	0.9947
MTF-GLP-HPM	16.8838	0.9669	1.4274	0.9660	0.0422	0.9944
ATPRK	**14.9425**	**0.9733**	**1.2814**	**0.9722**	**0.0412**	**1**
AATPRK	15.2378	0.9720	1.3209	0.9717	0.0425	**1**

3) Analysis of local window size for regression modelling in AATPRK. The local window size should be set to an appropriate value. Five window sizes, *W*=3, 5, 7, 9 and 11, were tested for AATPRK. The Hong Kong WorldView-2 dataset was used for analysis and the quantitative assessment is provided in Table 4. It is seen that when a 5 by 5 local window is used, a satisfactory accuracy can be produced and the increase in the local window size does not necessarily lead to an increase in pan-sharpening accuracy.

Table 4 Influence of the local window size for regression modelling in AATPRK (Hong Kong WorldView-2 dataset)

	RMSE	CC	ERGAS	UIQI	SAM
ATPRK	14.0129	0.9776	1.1768	0.9773	0.0414
AATPRK (3×3)	13.7926	0.9785	1.1597	0.9784	0.0396
AATPRK (5×5)	**13.4886**	**0.9794**	**1.1322**	**0.9793**	**0.0387**
AATPRK (7×7)	13.6094	0.9790	1.1422	0.9788	0.0390
AATPRK (9×9)	13.7349	0.9786	1.1525	0.9784	0.0394
AATPRK (11×11)	13.8696	0.9782	1.1636	0.9780	0.0399

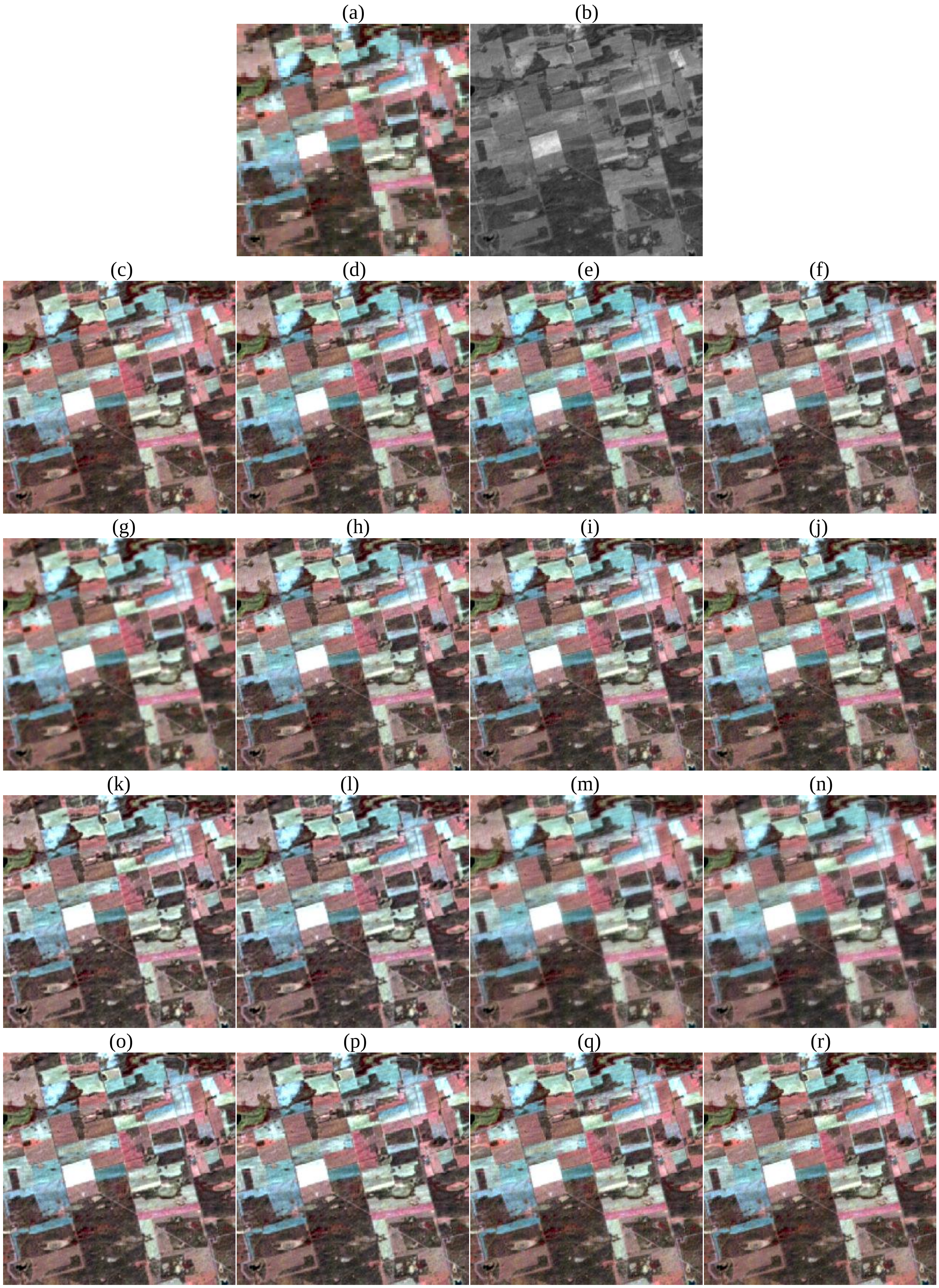

Fig. 8. Pan-sharpening results for the Landsat ETM+ dataset (bands 4, 3 and 2 as RGB). (a) 60 m coarse image. (b) 30 m PAN image. (c) 30 m reference image. (d) PCA. (e) GS. (f) GSA. (g) PRACS. (h) HPF. (i) SFIM. (j) Indusion. (k) ATWT. (l) AWLP. (m) ATWT-M2. (n) ATWT-M3. (o) MTF-GLP. (p) MTF-GLP-HPM. (q) ATPRK. (r) AATPRK.

3.4. Experiment on the Landsat ETM+ dataset

In this experiment, the performances of ATPRK and AATPRK are illustrated by the Landsat ETM+ dataset. Fig. 8 exhibits the results for a 200 by 200 sub-area of the studied area. As shown in the figure, PRACS, ATWT-M2 and ATWT-M3 produced over-smooth results and failed to restore the heterogeneous variation, while PCA, GS, ATWT and AWLP have poor performances in preserving the spectral properties. Table 5 shows the corresponding quantitative assessment results. Similarly to the previous tests, ATPRK is superior to the 13 benchmark methods in terms of all six indices. For example, the RMSE value of ATPRK is 1.3582, whereas the benchmark methods generally produced RMSEs greater than 1.5; the ERGAS of ATPRK is less than 2, while the benchmark methods produced values greater than 2. Moreover, compared to ATPRK, AATPRK is more accurate in this experiment. The reason is that the studied scene contains much local variation, as can be observed from Fig. 3(c). Thus, ATPRK can be enhanced with the local scheme in AATPRK.

Table 5 Quantitative assessment of the pan-sharpening methods for the Landsat ETM+ dataset

	RMSE	CC	ERGAS	UIQI	SAM(°)	Coherence
Ideal	0	1	0	1	0	1
PCA	1.4847	0.9746	2.0193	0.9718	0.0238	0.9960
GS	1.5903	0.9708	2.1642	0.9675	0.0238	0.9923
GSA	1.9047	0.9730	2.5784	0.9643	0.0257	0.9945
PRACS	1.4497	0.9764	1.9615	0.9752	0.0259	0.9981
HPF	1.5463	0.9724	2.1024	0.9723	0.0239	0.9956
SFIM	1.5448	0.9725	2.1005	0.9723	0.0237	0.9956
Indusion	2.2080	0.9446	2.9939	0.9440	0.0296	0.9738
ATWT	1.8304	0.9682	2.4833	0.9647	0.0253	0.9876
AWLP	1.9089	0.9682	2.5850	0.9642	0.0269	0.9875
ATWT-M2	1.4892	0.9736	2.0309	0.9715	0.0282	0.9917
ATWT-M3	1.5871	0.9718	2.1534	0.9693	0.0309	0.9906
MTF-GLP	1.6020	0.9719	2.1777	0.9710	0.0241	0.9927
MTF-GLP-HPM	1.6091	0.9718	2.1875	0.9708	0.0237	0.9926
ATPRK	1.3582	0.9776	1.8504	0.9776	**0.0230**	**1**
AATPRK	**1.3333**	**0.9785**	**1.8190**	**0.9785**	0.0236	**1**

4. DISCUSSION

4.1.ATPRK and AATPRK

As an extension of ATPRK, AATPRK inherits the advantages of ATPRK. It accounts explicitly for the size of support, spatial correlation, and the PSF of the sensor. Moreover, it can also precisely preserve the spectral properties of the original coarse data, as shown in Tables 2, 3 and 5. The theoretical proof of coherence characteristic of AATPRK runs parallel to the proof presented in Wang et al. (2015). The experimental results show that both ATPRK and AATPRK outperform the 13 compared benchmark methods summarized in Vivone et al. (2015). The two geostatistical approaches produced RMSE, ERGAS, SAM, CC and UIQI values closer to the ideal ones. The experiments demonstrated the great utility of ATPRK and AATPRK in pan-sharpening.

As illustrated in the experiments, AATPRK tends to be more advantageous when the scene is spatially locally varying, such as that in the Hong Kong WorldView-2 image and the Landsat ETM+ image. Essentially, in ATPRK, the geostatistical process is implemented in the second step, this is, ATPK-based residual downscaling. The residual image is required to be as stationary as possible to meet the stationary assumption in the kriging interpolation. When the studied scene is locally varying, the global regression model in ATPRK may not be able to sufficiently characterize the relationship between the coarse and PAN bands and, as a result, the generated residuals may vary greatly from area to area (i.e., require a non-stationary model). With the regression model fitted on a coarse pixel basis in AATPRK, where pixels in the local window rather than in the entire image are considered, the generated residual images show less local variation, as shown in Fig. 5. The local non-stationary scheme, therefore, can lead to residuals that are more suited to manipulation with a stationary model.

AATPRK fits the regression model for each coarse pixel. It is necessary to compare the computational complexity of the two approaches. Table 6 lists the computing time in the experiments on the two types of datasets. All experiments were carried out on an Intel Core i7

Processor at 3.40 GHz with the MATLAB 7.1 version. The computing time of the pan-sharpening algorithms is closely related to the spatial size of the image, number of bands and the spatial resolution ratio between the coarse and PAN bands (i.e., zoom factor). It is clear that AATPRK takes more time than ATPRK.

Table 6 Computational cost of ATPRK and AATPRK for the used datasets

	Size of coarse images	Zoom factor	Number of bands	ATPRK	AATPRK
WorldView-2	125×125	4	8	137s	327s
Landsat	256×256	2	3	21s	455s

4.2.Local ATPK

In AATPRK, residual downscaling is performed by global ATPK. This is distinguished from Pardo-Iguzquiza et al. (2011), in which a local scheme was developed for kriging interpolation. In local ATPK interpolation, semivariogram deconvolution for parameterizing the RF model and the kriging weights calculation are carried out for each coarse pixel. This is computationally intensive, especially for large areas with a large number of pixels. In view of this, we applied global ATPK instead. Nevertheless, local ATPK has potential for possible enhancement of the AATPRK approach proposed in this paper. Thus, any strategy able to decrease the computational cost of local ATPK should be encouraged. For example, kriging interpolation can be performed in units of non-overlapping blocks that covers S by S pixels and, correspondingly, computational cost can be decreased by S^2 times. This amounts to dividing the entire study area into sub-areas. In this case, the determination of S, which could also be spatially adaptive, would be a critical issue.

4.3.Multiple covariates

With respect to the pan-sharpening issue, the PAN band is used as the single covariate in ATPRK and AATPRK. In fact, both approaches can incorporate readily other supplementary data for possible enhancement. The relationship between the multiple covariates and observed coarse data can be built via multiple regression, which can be achieved by extending (3) and (14). In view of the ease of incorporating multiple covariates, more relevant information (e.g., topographic maps, thematic maps, field measurements) on the studied areas is encouraged to be sought in future research.

5. Conclusion

It is a natural objective to merge the information in different wavebands with different spatial resolutions from the same satellite. This paper presents two geostatistical solutions for pan-sharpening; ATPRK and AATPRK. Both approaches first perform regression of each coarse band on the PAN band and then use ATPK to downscale the band residuals from the regression models. Different from ATPRK that uses a global regression model, AATPRK fits the regression model with a local scheme. The relationship between the coarse and PAN bands in AATPRK is modelled on a coarse pixel basis and the regression coefficients change across the image.

Experiments were carried out on three experimental cases, two WorldView-2 datasets and one Landsat ETM+ dataset, in which the two geostatistical solutions were compared to 13 benchmark algorithms. The findings are summarized as follows.

1) Both ATPRK and AATPRK outperformed the 13 benchmark algorithms, demonstrating their great utility for pan-sharpening.
2) Unlike the benchmarks, both ATPRK and AATPRK have the characteristic of perfect coherence with the original coarse data.
3) Where the residuals produced by a single, global regression model in ATPRK are locally varying, the advanced ATPRK approach can be further enhanced by its non-stationary extension, AATPRK.

Acknowledgment

This work was supported in part by the Research Grants Council of Hong Kong under Grant PolyU 15223015 and Grant PolyU 5249/12E, in part by the National Natural Science Foundation of China under Grant 41331175, in part by the Leading talent Project of National Administration of

Surveying under grant K.SZ.XX.VTQA, and in part by the Ministry of Science and Technology of China under Grant 2012BAJ15B04 and Project 2012AA12A305. The authors would like to thank the authors in Vivone et al. (2015) for sharing their code for pan-sharpening algorithms at http://www.openremotesensing.net. PMA is grateful to the University of Utrecht for supporting him with The Belle van Zuylen Chair.

References

Aiazzi, B., Alparone, L., Baronti, S., Garzelli, A., Selva, M., 2006. MTF-tailored multiscale fusion of high-resolution MS and Pan imagery. Photogrammetric Engineering and Remote Sensing 72(5), 591–596.

Aiazzi, B., Baronti, S., Selva, M., 2007. Improving component substitution pansharpening through multivariate regression of MS+Pan data. IEEE Transactions on Geoscience and Remote Sensing 45(10), 3230–3239.

Atkinson, P. M., Pardo-Igúzquiza, E., Chica-Olmo, M., 2008. Downscaling cokriging for super-resolution mapping of continua in remotely sensed images. IEEE Transactions on Geoscience and Remote Sensing 46(2), 573–580.

Atkinson, P. M., 2013. Downscaling in remote sensing. International Journal of Applied Earth Observation and Geoinformation 22, 106-114.

Chavez Jr., P. S., Sides, S. C., Anderson, J. A., 1991. Comparison of three different methods to merge multiresolution and multispectral data: Landsat TM and SPOT panchromatic. Photogrammetric Engineering and Remote Sensing 57(3), 295–303.

Cheng, J., Liu, H., Liu, T., Wang, F., Li, H., 2015. Remote sensing image fusion via wavelet transform and sparse representation. ISPRS Journal of Photogrammetry and Remote Sensing 104, 158–173.

Choi, J., Yu, K., Kim, Y., 2011. A new adaptive component-substitution based satellite image fusion by using partial replacement. IEEE Transactions on Geoscience and Remote Sensing 49(1), 295–309.

Gillespie, A. R., Kahle, A. B., Walker, R. E., 1987. Color enhancement of highly correlated images—II. Channel ratio and "Chromaticity" transform techniques. Remote Sensing of Environment 22(3), 343–365.

Hengl, T., Heuvelink, G. B. M., Stein, A., 2004. A generic framework for spatial prediction of soil variables based on regression-kriging. Geoderma 120, 75–93.

Hengl, T., Heuvelink, G. B. M., Rossiter, D. G., 2007. About regression-kriging: From equations to case studies. Computers & Geosciences 33, 1301–1315.

Khan, M. M., Chanussot, J., Condat, L., Montavert, A., 2008. Indusion: Fusion of multispectral and panchromatic images using the induction scaling technique. IEEE Geoscience and Remote Sensing Letters 5(1), 98–102.

Kitanidis, P., 1994. Generalized covariance functions in estimation. Mathematical Geology 25, 525–540.

Kyriakidis, P. C., Yoo, E.-H., 2005. Geostatistical prediction and simulation of point values from areal data. Geographical Analysis 37(2), 124–151.

Kyriakidis, P. C., 2004. A geostatistical framework for area-to-point spatial interpolation. Geographical Analysis 36(3), 259–289.

Laben, C. A., Brower, B. V., 2000. Process for enhancing the spatial resolution of multispectral imagery using pan-sharpening. U.S. Patent 6011875.

Lee, J., Lee, C., 2010. Fast and efficient panchromatic sharpening. IEEE Transactions on Geoscience and Remote Sensing 48(1), 155–163.

Liu, J. G., 2000. Smoothing filter based intensity modulation: A spectral preserve image fusion technique for improving spatial details. International Journal of Remote Sensing 21(18), 3461–3472.

Nunez, J., Otazu, X., Fors, O., Prades, A., Pala, V., Arbiol, R., 1999. Multiresolution-based image fusion with additive wavelet decomposition. IEEE Transactions on Geoscience and Remote Sensing 37(3), 1204–1211.

Pardo-Igúzquiza, E., Chica-Olmo, M., Atkinson, P. M., 2006. Downscaling cokriging for image sharpening. Remote Sensing of Environment 102(2), 86–98.

Pardo-Iguzquiza, E., Rodríguez-Galiano, V. F., Chica-Olmo, M., Atkinson, P. M., 2011. Image fusion by spatially adaptive filtering using downscaling cokriging. ISPRS Journal of Photogrammetry and Remote Sensing 66(3), 337–346.

Pohl, C., Van Genderen, J. L., 1998. Multisensor image fusion in remote sensing: concepts, methods and applications. International Journal of Remote Sensing 19(5), 823–854.

Ranchin, T., Wald, L., 2000. Fusion of high spatial and spectral resolution images: The ARSIS concept and its implementation. Photogrammetric Engineering and Remote Sensing 66(1), 49–61.

Sales, M. H. R., Souza, Jr., C. M., Kyriakidis, P. C., 2013. Fusion of MODIS images using kriging with external drift. IEEE Transactions on Geoscience and Remote Sensing 51(4), 2250–2259.

Shettigara, V. K., 1992. A generalized component substitution technique for spatial enhancement of multispectral images using a higher resolution data set. Photogrammetric Engineering and Remote Sensing 58(5), 561–567.

Tang, Y., Atkinson, P. M., Zhang, J., 2015. Downscaling remotely sensed imagery using area-to-point cokriging and multiple-point geostatistical simulation. ISPRS Journal of Photogrammetry and Remote Sensing 101, 174–185.

Tu, T.-M., Su, S.-C., Shyu, H.-C., Huang, P. S., 2001. A new look at IHS-like image fusion methods. Information Fusion 2(3), 177–186.

Vivone, G., Restaino, R., Dalla Mura, M., Licciardi, G., Chanussot, J., 2014. Contrast and error-based fusion schemes for multispectral image pan-sharpening. IEEE Geoscience and Remote Sensing Letters 11(5), 930–934.

Vivone, G., Alparone, L., Chanussot, J., Dalla Mura, M., Garzelli, A., Licciardi, G. A., Restaino, R., Wald, L., 2015. A critical comparison among pansharpening algorithms. IEEE Transactions on Geoscience and Remote Sensing 53(5), 2565–2586.

Wald, L., Ranchin, T., Mangolini, M., 1997. Fusion of satellite images of different spatial resolutions: assessing the quality of resulting images. Photogrammetric Engineering and Remote Sensing 63(6), 691–699.

Wang, Q., Shi, W., Zhang, H., 2014. Class allocation for soft-then-hard subpixel mapping algorithms with adaptive visiting order of classes. IEEE Geoscience and Remote Sensing Letters 11(9), 1494–1498.

Wang, Q., Shi, W., Atkinson, P. M., Zhao, Y., 2015. Downscaling MODIS images with area-to-point regression kriging. Remote Sensing of Environment 166, 191–204.

Wang, Z., Bovik, A. C., 2002. A universal image quality index. IEEE Signal Processing Letters 9(3), 81–84.

Wang, Z., Ziou, D., Armenakis, C., Li, D., Li, Q., 2005. A comparative analysis of image fusion methods. IEEE Transactions on Geoscience and Remote Sensing 43(6), 1391–1402.

Zhang, Y., Mishra, R. K., 2014. From UNB PanSharp to FuzeGo— the success behind the pan-sharpening algorithm. International Journal of Image and Data Fusion 5(1), 39-53.

Zhang, J., 2010. Multi-source remote sensing data fusion: status and trends. International Journal of Image and Data Fusion 1(1), 5-24.

Zhou, X., Liu, J., Liu, S., Cao, L., Zhou, Q., Huang H., 2014. A GIHS-based spectral preservation fusion method for remote sensing images using edge restored spectral modulation. ISPRS Journal of Photogrammetry and Remote Sensing 88, 16–27.